lubricants

MDPI

Article

Surface Characterization of Cylinder Liner–Piston Ring Friction Pairs Under Different Temperature and Load by Power Spectral Density Method

Xiaori Liu [1], Xiaofei Cao [1], Xuan Ma [2] and Menghan Li [1,*]

[1] School of Energy and Environmental Engineering, Hebei University of Technology, Tianjin 300401, China; liuxiaori@hebut.edu.cn (X.L.); 202331305027@stu.hebut.edu.cn (X.C.)
[2] Department of Test and Development Engineering, Caterpillar (China) Co., Ltd., Wuxi 214028, China; max.ma1@cat.com
* Correspondence: limenghan@hebut.edu.cn

Abstract: Piston ring–cylinder liner is one of the most important friction pairs in internal combustion engines. The surfaces of the piston ring and the cylinder liner are affected by high temperature and high pressure, and the influence mechanism of temperature and pressure on their microscopic morphology parameters is yet to be revealed. In this paper, high temperature friction and wear experiments on the piston ring and cylinder liner are carried out to obtain the microscopic morphology of the cylinder liner and piston ring at different temperatures and pressures, and their changes under different temperatures and pressures are investigated by using two methods, namely, fractal dimension and three-dimensional surface roughness characterization. The results show that, as the temperature increases, the texture patterns on the cylinder liner's friction surface become simpler, with the fractal dimension showing a decreasing trend while the roughness shows an increasing trend. Compared to the condition at 80 °C, the surface roughness (Sa) of the cylinder liner increased by approximately 58.43% at 190 °C, while that of the piston ring increased by about 96.5%. With increasing pressure, both the fractal dimension and the roughness of the friction surface first decrease and then increase.

Keywords: piston ring; cylinder liner; surface characterization; power spectral density method; various operating conditions

check for updates

Received: 14 April 2025
Revised: 14 May 2025
Accepted: 17 May 2025
Published: 25 May 2025

Citation: Liu, X.; Cao, X.; Ma, X.; Li, M. Surface Characterization of Cylinder Liner–Piston Ring Friction Pairs Under Different Temperature and Load by Power Spectral Density Method. *Lubricants* **2025**, *13*, 237. https://doi.org/10.3390/lubricants13060237

Copyright: © 2025 by the authors. Licensee MDPI, Basel, Switzerland. This article is an open access article distributed under the terms and conditions of the Creative Commons Attribution (CC BY) license (https://creativecommons.org/licenses/by/4.0/).

1. Introduction

The friction loss of the cylinder liner–piston ring is one of the most significant mechanical losses in an internal combustion engine. According to statistics, about 20–40% of engine friction loss occurs on the cylinder liners and piston rings [1,2]. Due to the reciprocating motion of the piston in the cylinder liner, the first piston ring begins the operating phase with quick changes in temperature and pressure at the contact surface, following the high temperature and pressure near the top dead center (TDC) position. The frictional properties of the cylinder liner and piston ring also show complex characteristics with the rapidly changing working conditions [3,4].

Temperature has a significant impact on the friction and wear of the piston ring and cylinder liner. The study by Shahmohamadi et al. [5] showed that in-cylinder combustion leads to high temperatures at the top of the cylinder liner and low temperatures at the bottom, and that the temperature difference of the cylinder liner's surface at the contact range of the piston ring can reach a temperature span of more than 50 °C. The temperature of the engine cylinder liner has a significant effect on the frictional power consumption of the piston ring, where the difference in frictional power consumption even reaches nearly 50% in the studied temperature range. Meanwhile, the optimal operating temperature exists on the surface of both the cylinder liner and the piston ring to reduce the frictional loss of the piston ring [6,7]. It was found that the effect of temperature on friction was mainly reflected in the variation in grease viscosity with temperature during actual friction. Du Chang et al. [8] conducted experimental studies on the effects of temperature and lubricating oil on the friction performance of cylinder liner–piston ring (CL-PR) systems. Their research revealed that the wear of the friction pair reached its most severe state at 120 °C, with the predominant wear mechanisms being identified as abrasive wear and adhesive wear. Wolff et al. [9] set the lubricating oil at constant temperatures of 93 °C and 200 °C. The results indicate that, when either the cylinder liner or lubricant temperature is relatively low, the hydrodynamic friction power consumption of piston rings is more significant. At higher temperatures, while the hydrodynamic friction power consumption decreases, the rough contact friction power consumption increases significantly. Zhang Xiang et al. [10] designed six temperature distribution schemes for cylinder liners, achieving a 34.4% reduction in maximum friction loss compared to the original engine configuration. Valiente-Blanco et al. [11] studied the coefficient of friction (COF) of polytetrafluoroethylene (PTFE) grease lubricated bushings with Ti6Al4 V alloy shafts at 200 °C. LYU et al. [12] combined the growth and wear model of the tribofilm caused by zinc dialkyl dithiophosphate (ZDDP) with the temperature field. The results showed that the growth rate of the tribofilm appears to be more dependent on the temperature than on the contact pressure. In addition to the temperature, the external load, speed, and roughness of the friction pair also have an effect on the contact characteristics of the friction pair [13–15]. Bewsher's study [16] showed that the lubrication state of the engine's friction pair is dominated by boundary lubrication during the combustion stroke and investigated the effect of combustion products, as well as frictional reaction film, on the frictional characteristics under high-pressure conditions. Zhang et al. [17] divided the wear states of the cylinder liner and piston ring into mild wear state, medium wear state, and severe wear state, which varied with the operating parameters.

When analyzing the surface wear morphology of piston rings and cylinder liners, geometry-related parameters like roughness, wear depth, wear rate, fractal dimension, and so on are utilized for parameterization. This allows for a more quantitative and in-depth understanding of the wear characteristics, facilitating comparisons between different wear states and providing a basis for further research on tribological properties and the durability of these components [18–20]. Zhang et al. [21] measured the change in wear rate at different speeds and pressures to build the wear map. Liu et al. [22] optimized the double-sided textured CLPR; a maximum reduction in the friction coefficient of 12.63% was achieved compared to the untextured surface, with corresponding reductions in the wear depth of the cylinder liner and piston ring of 16.73% and 18.25%. Lang et al. [23] carried out a piston ring–cylinder liner wear test based on different speeds and pressures to obtain a 2D cylinder liner morphology profile and performed a 2D fractal dimension and roughness analysis for the cylinder liner. To sum up, the three-dimensional microfractal characteristics and laws of piston rings and cylinder liners under different

operating conditions need to be further investigated. The changes in microscopic morphology can be characterized using the fractal method. The fractal characteristics mean that the similarity exists in the detailed features of the surface morphology at different scales, indicating that the rough surface has self-similarity and scale-invariance [24–26]. As a result, the morphological aspects of the rough surface may be described using the fractal function. Pitchumani et al. [27] employed a two-dimensional fractal model to characterize wettability on randomly rough surfaces. Wujun Feng et al. [28] further integrated wavelet filters with fractal theory to analyze the surface morphology of titanium alloys, establishing a correlation between fractal dimension and surface roughness. Their research on micro-electrical discharge machining processes revealed that, under constant discharge duration, the fractal dimension increases with decreasing discharge energy. Correspondingly, the elevation in fractal dimension was found to be associated with an increasing trend in surface roughness. Mahmood et al. [29] combined the roughness parameters and fractal parameters to establish a three-dimensional formula for the fractal surface morphology formed in the cold-rolled workpiece and rolls based on the two-dimensional W-M model. Zhao et al. [30] used the box-width transformation method to calculate the fractal parameters of the friction bond surface of aluminum and magnesium metals under different welding processes, indicating that the fractal dimension, as an indicator to characterize the surface quality of their joints, is greatly affected by the variation of process parameters. Yi et al. [31] proposed a fretting damage model based on fractal theory and used the Weierstrass–Mandelbrot function in fractal theory to represent the rough contact surface. Eftekhari et al. [32] quantified parameters such as the fractal dimension, Hurst index with application of power spectral density data fitting fractal model, and root mean square roughness to investigate the surface morphological characteristics of sputtered yttria-stabilized zirconia (YSZ) films at different annealing temperatures.

Based on the above research findings, there exists a certain correlation between the fractal dimension and surface roughness of friction interfaces. Meanwhile, studies on the three-dimensional microscopic fractal characteristics and evolution patterns of piston rings and cylinder liners under varying operating conditions remain relatively scarce. Currently, there are limited investigations employing power spectral density (PSD) methods to analyze piston rings while simultaneously considering fractal parameter variations under multiple operating conditions involving temperature and pressure changes. To investigate the influence of different operating parameters on surface microtopography in cylinder liner–piston ring friction pairs under various working conditions, this study adopts a sectioned specimen testing approach. High-temperature tribological experiments are conducted under different temperature and pressure conditions to obtain the friction coefficient data and microscopic morphology characteristics of the friction pair. The three-dimensional surface topography is processed using power spectral density analysis, combined with fractal model fitting, to study the evolution patterns of microtopography with the operating parameters. Figure 1 shows the schematic diagram of the research approach in this paper.

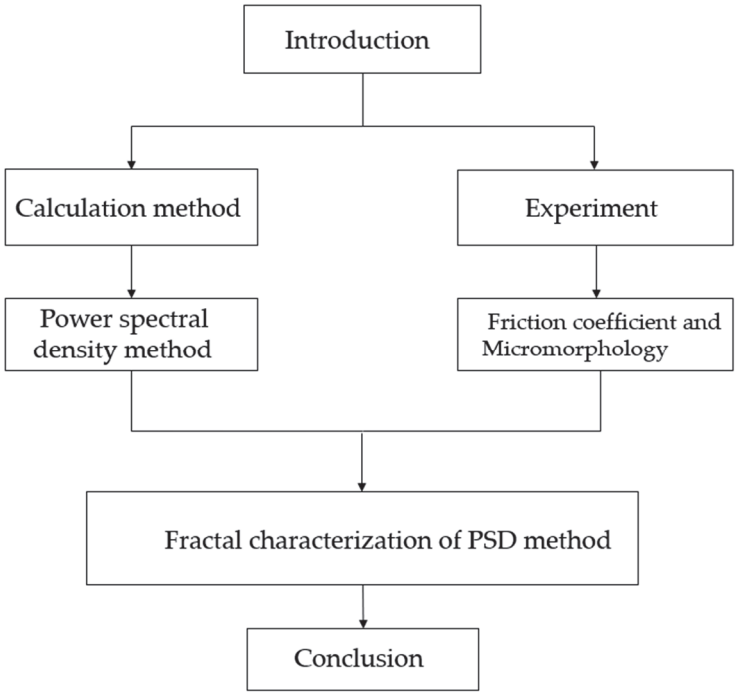


Figure 1. The schematic diagram of the research approach in this article.

2. Calculation Method and Validation

2.1. Calculation Principle of Fractal Dimension

The fractal dimension is calculated by processing the whole morphology using different measurement scales to obtain the equation of the scaling relationship of the morphological parameters.

The equation for the morphological measure and measurement scale can be expressed as [33]:

$$Q(\delta) = c\delta^{\alpha} \tag{1}$$

where Q is the morphological measure, and δ is the measurement scale. Both c and α are constants.

The fractal dimension of the profile is obtained by constructing a log–log coordinate of Q and δ. Then, a linear fit is made to the dimensional and scaling relationships calculated for the dimension, and a linear equation is established. The fractal dimension of the measured shape is obtained by the slope of the fitted equation.

Three principal methodologies are commonly employed for fractal dimension calculation: the box-counting method, the structure function method, and the power spectral density method. The box-counting method operates by systematically covering a surface with grids of progressively reduced box sizes, quantifying the total number of boxes required for full coverage, and deriving the fractal dimension through statistical regression of the logarithmic relationship between the box count and scale. The structure function method treats two-dimensional profile curves as stochastic time-series data, calculating the fractal dimension by analyzing variance increments across spatial displacements along the horizontal coordinate axis. The PSD method leverages Fourier spectral analysis to decompose surface height variations into spatial frequency components, with the fractal dimension calculated from the power-law scaling of the frequency–amplitude relationship. In this study, a comparative evaluation of the box-counting and PSD methods was conducted under controlled tribological conditions. The analytical results revealed superior robustness and resolution of the PSD method in characterizing multiscale surface degrada-

tion patterns. Consequently, the PSD method was selected for a systematic investigation of microtopographical evolution mechanisms in piston ring–cylinder liner systems.

2.2. Box-Counting Method

The box-counting method is one of the most widely used algorithms in fractal dimension calculation methods. Its calculation principle is, for the calculation of the fractal dimension of a two-dimensional graph, assume that there is a box with side length r. Cover the two-dimensional curve image to be measured with the box, where the box covering the curve to be measured is recorded as a non-empty box, and calculate the number of non-empty boxes, recorded as $S(r)$. Then, gradually reduce the scale r and repeatedly calculate the number of non-empty boxes $S(r)$ covering the image at the current scale to get the array of $(\log(r), \log S(r))$. When r is infinitely close to 0, the box-counting dimension of the curve graph can be calculated. In the calculation, the slope K of this functional relationship can be obtained using linear regression, counting the box dimension $D = -K$. The fractal dimension D calculated by the box-counting dimension method can be expressed as follows:

$$D = -\lim_{r \to 0} \frac{\log S(r)}{\log(r)} \tag{2}$$

The calculation of the fractal dimension of a three-dimensional surface is generalized from the principle of two-dimensional calculation. When the figure to be measured is a three-dimensional surface F, assume that there is a cubic box with side length r, cover the three-dimensional surface with boxes of that scale, and finally, arrive at the number of boxes $S(r)$ required to cover the surface. The box-counting dimension of the surface is calculated as in Equation (3) [34].

$$D(F) = -\lim_{r \to 0} \frac{\log S(r)}{\log(r)} \tag{3}$$

2.3. Power Spectral Density Method

The power spectral density method is mainly used for the processing of random time series signals. Extending this to the calculation of fractal dimension, the spatial frequency f of its signal sequence is the scale in the calculation of the fractal dimension. For rough surfaces with the fractal characteristics of contour curves, the fractal dimension is calculated as follows. Calculate the PSD $P(f)$ after processing the discrete data of the contour height of the 2D or 3D shape. The variation in power spectral density $P(f)$ and frequency f of the shape to be measured is plotted as a log-log graph, and it is judged whether the power spectral density $P(f)$ and frequency f satisfy $P(f) \in f^{(-\beta)}$. The exponent β is related to the calculated fractal dimension.

The PSD method can be used to calculate the fractal dimension of three-dimensional surfaces, in addition to the fractal dimension of two-dimensional curves. In the calculation of three-dimensional microscopic morphology, the two-dimensional power spectral density (area power spectral density, APSD) can be used, which is calculated using the Fourier transform autocorrelation function.

The two-dimensional Fourier transform is expanded along the x and y directions of the surface to be measured, so that a three-dimensional surface can be represented in the Cartesian coordinate system by the $z(x, y)$ function, where z refers to the actual height value at (x, y). Since the collected height data are not a continuous signal value, it is necessary to discretize the data when performing the processing. This method of Fourier transforming a

finite number of discrete data is the discrete Fourier transform (DFT). The two-dimensional discrete Fourier transform equation is as follows [32]:

$$H(f_x, f_y) = \sum_{f_x=0}^{M-1} \sum_{f_y=0}^{N-1} z(x,\ y) \mathrm{e}^{-i2\pi(T_x f_x x + T_y f_y y)} \tag{4}$$

where f_x and f_y denote the frequencies in the x and y directions, $f_x = 1/i\ T_x$, $fy = 1/i\ T_y$, $i = 1, 2...M$; T_x and T_y are the fixed intervals of sampling points in the x and y directions, respectively, $Tx = Ty$; and M and N are the number of sampling points in the x and y directions.

The 2D PSD can be estimated using a periodogram, and the discrete power spectral density can be approximated by Equation (5):

$$P\left(f_x,\ f_y\right) = \frac{1}{\mathrm{MN} T_x T_y} \left| H\left(f_x,\ f_y\right) \right|^2 \tag{5}$$

After PSD calculation, P and f are related by a power function:

$$P(f) = \alpha f^{\ -\beta} \tag{6}$$

Then, taking logarithms for both sides of the above equation:

$$\log(P) = \log(\alpha) - \beta \log(f) \tag{7}$$

where both α and β are fitting parameters. β and the fractal dimension D have the following relationship:

$$D = \begin{cases} 3 & 0 \le |\beta| \le 1 \\ (7 - |\beta|)/2 & 1 \le |\beta| \le 3 \\ 0 & |\beta| > 3 \end{cases} \tag{8}$$

2.4. Validation of Methods

After Mandelbrot founded fractal geometry, scholars in related fields proposed the Weierstrass–Mandelbrot fractal function (W-M function) for constructing two-dimensional fractal curves. On this basis, most of the methods for establishing 3D rough surfaces were to obtain fractal contour curves by 2D W-M fractal functions and then extend to the whole rough surface, which has great limitations in accurately characterizing 3D contour surfaces, fractal characterization, and the simulation of rough surfaces. With the development of fractal theory, subsequent scholars have established W-M functions on a three-dimensional scale to simulate the microscopic morphology of the constructed rough surface, which provides an important tool for the study of the contact mechanics of micro-convex bodies and the study of frictional wear properties of material surfaces.

The W-M function can accurately reflect the morphological characteristics of the rough surface constructed with theoretical fractal dimensions and feature scales. Yan and Komvoulos et al. [35] studied the fractal characteristics of three-dimensional rough surfaces and established a W-M surface for three-dimensional forms, whose three-dimensional expression is given in Equation (9):

$$z(x,\ y) = L\left(\frac{G}{L}\right)\left(\frac{(\ln\gamma)}{O}\right)^{\frac{1}{2}} \sum_{m=1}^{0} \sum_{n=-\infty}^{\infty} \left\{ \cos(\phi_{m,n}) - \cos\left[\frac{2\pi\gamma^n \left(x^2 + y^2\right)^{\frac{1}{2}}}{L} \cos\left(\tan^{-1}\left(\frac{y}{x}\right) - \frac{\pi m}{O} \right) + \phi_{m,n} \right] \right\} \times \gamma^{(D_s\ -\ 3)n} \tag{9}$$

where $z(x, y)$ denotes the height value of the profile at (x, y). L is the sampling length. G is the scale factor. γ is the characteristic parameter, generally taken as 1.5. O denotes

the number of protruding folds on the constructed surface, and n is the frequency index. $\phi(m, n)$ is the random phase, taken as [0, 2π]. Ds is the theoretical fractal dimension, generally taken as $2 < Ds < 3$ for three-dimensional surfaces.

In practical engineering applications, the W-M function is generally used in its discrete form [36]:

$$z(x, y) = \sum_{n=1}^{\infty} C_n \gamma^{-(3-D_s)} \sin[\gamma^n (x\cos B_n + y\sin B_n) + A_n] \quad (10)$$

where Cn is a normally distributed random number obeying a mean of 0 and a variance of 1. An and Bn are mutually independent and obey random phases on [0, 2π].

The surfaces constructed by the W-M function have obvious fractal characteristics, so they can be used to verify the accuracy of the box-dimension method and the PSD method to calculate the fractal dimension. The W-M function surface is constructed in Matlab software (2020a version). For the theoretical fractal dimensions set Ds = 2.2, 2.4, 2.6, and 2.8, respectively, scale coefficients Cn = 0.001 and n = 100 were selected, plane coordinates x = [0.01, 1], and y = [0.01, 1] were taken, and the step size was 0.01, and the 3D rough surface was drawn as shown in Figure 2.

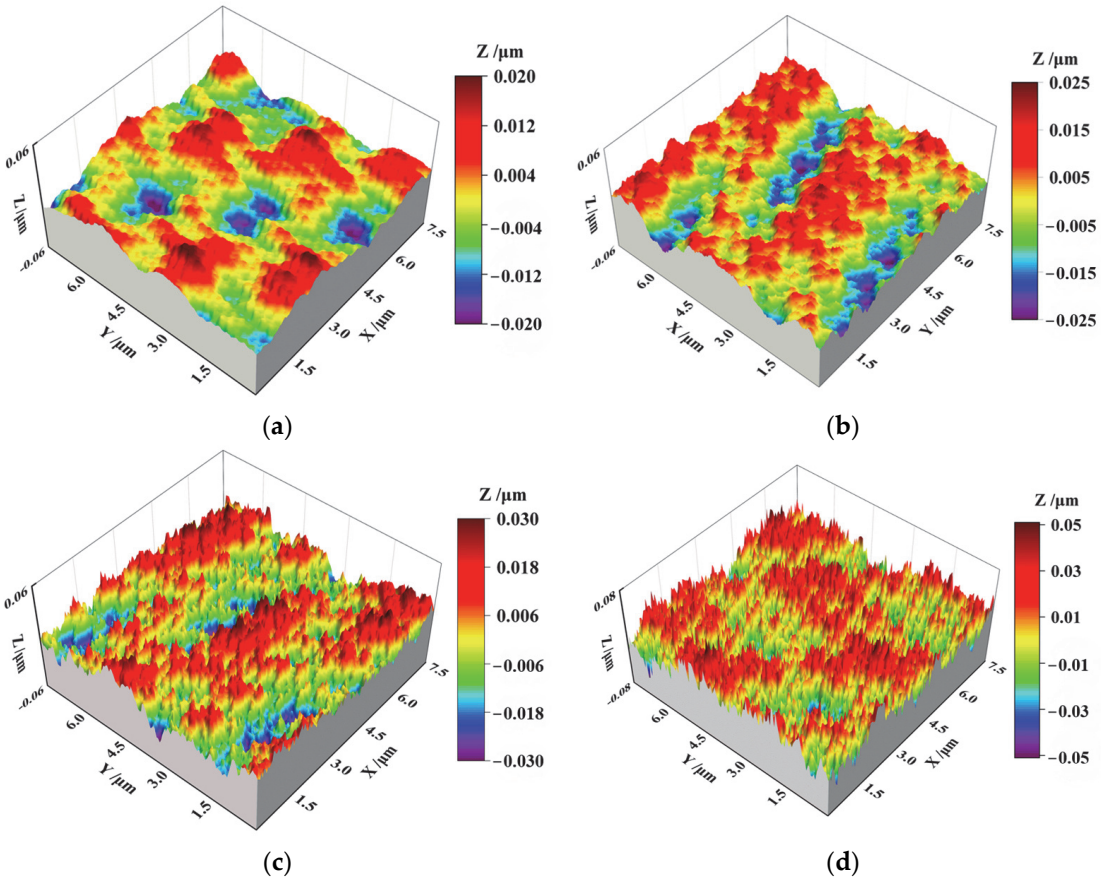


Figure 2. Three-dimensional surfaces constructed in different theoretical fractal dimensions: (**a**) Ds = 2.2, (**b**) Ds = 2.4, (**c**) Ds = 2.6, and (**d**) Ds = 2.8.

It is observed that there is a more obvious trend between the surface morphology and the fractal dimension. As the fractal dimension increases, the number of peaks and valleys increases and becomes more densely distributed, and the morphology tends to be more complex. It can also be seen from the figure that the maximum peak and minimum valley values of the morphology increase with the increase in the fractal dimension at the same feature scale G. The related results are shown in Table 1.

Table 1. Peak and valley values of profile height corresponding to theoretical fractal dimensions.

Theoretical Fractal Dimension	Maximum Peak Value (μm)	Minimum Valley Value (μm)
2.2	0.0220	−0.0231
2.4	0.0248	−0.0297
2.6	0.0394	−0.0389
2.8	0.0665	−0.0609

The local features of the morphology were more apparent with a low fractal dimension. As the fractal dimension increases, the feature similarity of each region of the morphology increases. That is, the self-similarity of the microscopic morphology increases with the increase in the fractal dimension.

Surfaces with fractal characteristics constructed from the W-M function can be used to verify the computational accuracy of the fractal dimension algorithm. Table 2 shows the fractal dimensions (D_f) and errors calculated by the box-counting dimension method and the PSD method.

Table 2. Calculation results of fractal dimension for both methods.

Theoretical Fractal Dimension	Box-Counting Method		PSD Method	
	D_f	Errors (%)	D_f	Errors (%)
2.2	2.211	0.50	2.262	2.82
2.4	2.453	2.21	2.443	1.79
2.6	2.531	2.65	2.572	1.08
2.8	2.594	7.36	2.822	0.79

As demonstrated in Table 2, the box-counting method exhibits higher computational accuracy at lower fractal dimensions, with errors remaining below 1%. However, when the theoretical fractal dimension exceeds 2.6, the calculated values from the box-counting method show minimal variation with the increasing theoretical dimensions. Notably, at a theoretical dimension of 2.8, the computed value remains below 2.6, indicating significant deviation. In contrast, the power spectral density method maintains a stable range of absolute errors across increasing theoretical dimensions, while the relative error decreases proportionally due to the scaling effect of higher theoretical values. Combining the above results and analysis, the PSD method is selected as the main method to calculate the fractal dimension of the 3D morphology.

3. Experiment

In this study, the friction pair of the first piston ring and cylinder liner, which is working under high temperature and pressure conditions, was selected for the determination of the variation of friction and wear behavior with temperature. The selected lubricant is the 15W-40 diesel engine lubricant produced by Mobil Corporation (Irving, TX, USA). The experiment was divided into two parts: the friction experiment and the morphological acquisition. The equipment used for the friction test was the SRV-V high temperature friction and abrasion tester (manufactured by Optimol Instruments Prüftechnik GmbH, Munich, Germany), and the other equipment used to collect morphological data was the VK-150K 3D laser microscopic imager (manufactured by Keyence Corporation, Osaka, Japan). The equipment is shown in Figure 3.

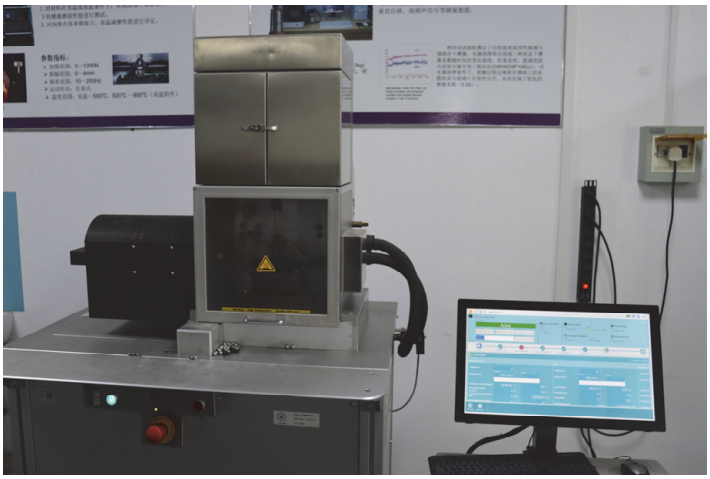


Figure 3. SRV-V high temperature friction and wear tester.

The SRV consists of a temperature control module, a mechanical module, software, and a test stand. During the friction process, the ambient temperature, friction load, and running speed may be regulated, and a variation curve of the friction coefficient with a time series can be obtained.

The experiments used the cut section of the cylinder liner and piston ring to simulate the friction behavior in real working conditions. The experimental materials were selected from the cylinder liner and piston ring components originally produced by the same model of diesel engine. Due to space constraints on the experimental bench, it was not possible to use complete cylinder liners and piston rings for the experiment. Therefore, according to the requirements of the experimental equipment, the cylinder liners and piston rings were cut, and experiments were conducted using cut samples. The cut samples of the piston rings and cylinder liners were selected with a straight-line spacing of 20 mm at both ends to ensure proper friction surface fit during assembly. When designing the constant temperature experiment, seven experimental temperature points were set between 80 °C and 300 °C. After the experiment, the coking status of each group of experiments was examined. The experimental samples at 80 °C, 110 °C, and 140 °C showed no obvious coking. The samples at 190 °C exhibited some coke deposits, while the samples at 230 °C, 270 °C, and 300 °C all had a significant amount of black coke deposits, which were difficult to remove during subsequent cleaning. At the same time, the friction coefficient fluctuated significantly at 230 °C, 270 °C, and 300 °C, and the transmission device and fixtures of the experimental bench exhibited noticeable vibrations. When designing the constant pressure experiment, the maximum contact load of the cylinder liner–piston ring friction pair near the top dead center of the diesel engine under study was 16.82 MPa, and the minimum load near the bottom dead center was 0.27 MPa. The loading range was calculated to be [20, 1200] N based on the actual area of the friction contact surface of the sample. Based on the above experimental phenomena, four constant temperature conditions ranging from 80 °C to 190 °C were selected for the constant temperature experiment. In the constant pressure experiment, loads of 300 N, 600 N, 900 N, 1200 N, and 1500 N were selected for the experiment. In constant temperature conditions, the friction test parameters were specified as 60 min sliding time and 0.14 m/s sliding speed for temperatures of 80 °C, 110 °C, 140 °C, and 190 °C. Under constant pressure conditions, tests were carried out at 300 N, 600 N, 900 N, 1200 N, and 1500 N while the sliding time and speed were the same as the fixed temperature condition. Table 3 shows the controlled parameters for the constant temperature and pressure experiments.

Table 3. Basic parameters of experiments.

Experimental Parameters	Constant Temperature	Constant Pressure
Pressure (N)	1200	300, 600, 900, 1200, 1500
Frequency (Hz)	20	20
Displacement (mm)	3	3
Sliding time (min)	60	60
Temperature (°C)	80, 110, 140, 190	190

After the friction experiments under different working conditions, the microscopic morphology of the cylinder liner and piston ring was collected by the 3D laser microscopic imager. The microscope imager is set to 2.66235×10^{-4} (μm/pixel) for planar accuracy and 1×10^{-4} (μm/pixel) for vertical accuracy.

4. Experimental Results and Discussion

4.1. Variation of Friction Coefficient

In the experimental groups with constant temperature or pressure, the variation curves of the friction coefficient for the experimental groups with constant temperature or pressure are shown in Figure 4.

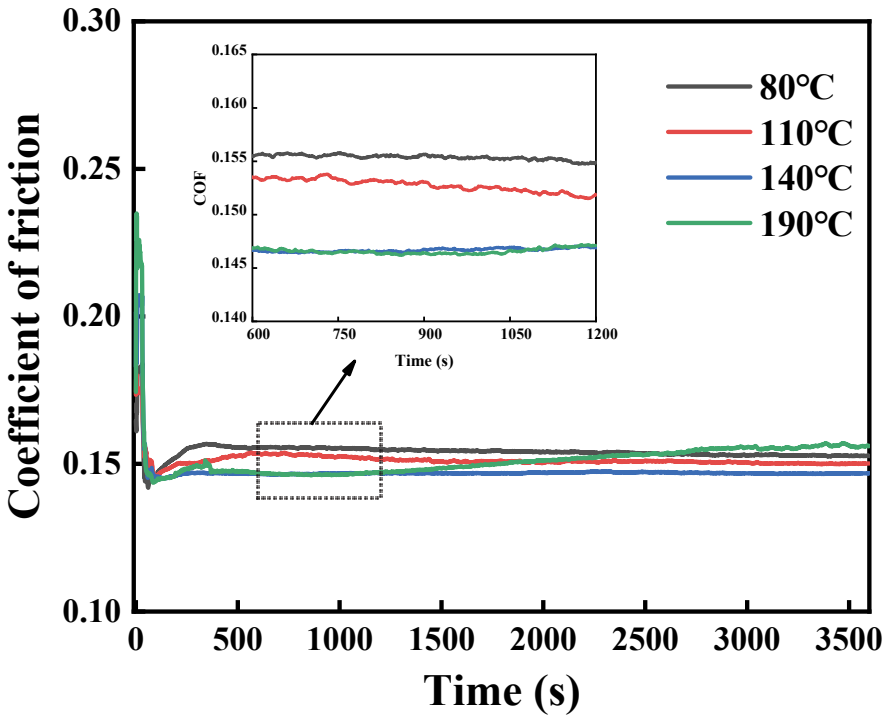


Figure 4. Variation process of friction coefficient under fixed temperature working conditions.

In the constant temperature experiments, the friction coefficients at all operating conditions showed large irregular changes within about 50 s after the start of the friction process. In the friction experiments at 190 °C, the high temperature resulted in local heat accumulation at the rough peak position, and some coking material was also present on the surface of the specimen after the experiment. After 1500 s of friction processes, the friction coefficient is already at the end of the stable stage. With the further increase in the friction time, the coking material accumulated, making the friction coefficient also show a slow increase. In the three sets of experiments at temperatures below 190 °C, the friction coefficient has always shown a stable state, and there is no obvious coking

phenomenon during the friction process because the experimental temperature is far below the deterioration temperature of the lubricant.

At the late friction stage, the friction coefficient at low-temperature operating conditions also shows a slightly decreasing trend after reaching the stable stage, mainly due to the presence of a small amount of friction-reducing additives in the lubricant. During these friction processes, the plastic stress and shear force increase, and a large amount of frictional heat is generated as the contact surface of the friction sub increases. The friction reaction film is gradually formed under the action of plastic stress and frictional heat, thus acting as a friction reduction.

Based on the above experimental phenomena, the average value of the coefficient of friction, calculated from the data within 600 s to 1200 s at the beginning of the experiment, was chosen as the typical data for characterizing the coefficient of friction at the corresponding temperature. The COFs in this region are shown in Table 4.

Table 4. The average friction coefficient of corresponding temperature conditions.

Temperature (°C)	Minimum COF	Maximum COF	Average COF
80	0.1543	0.1558	0.1552
110	0.1506	0.1538	0.1523
140	0.1464	0.1471	0.1468
190	0.1462	0.1470	0.1464

As shown in Table 4, the coefficient of friction at 80 °C is the largest in the constant temperature experiments at these four temperature points. When the temperature increases, the coefficient of friction decreases instead, while the coefficients of friction at 140 °C and 190 °C are similar.

The variation curves of the friction coefficient for each working condition in the constant pressure experiment are shown in Figure 5. Table 5 shows the peak and valley values of the COF variation in this region.

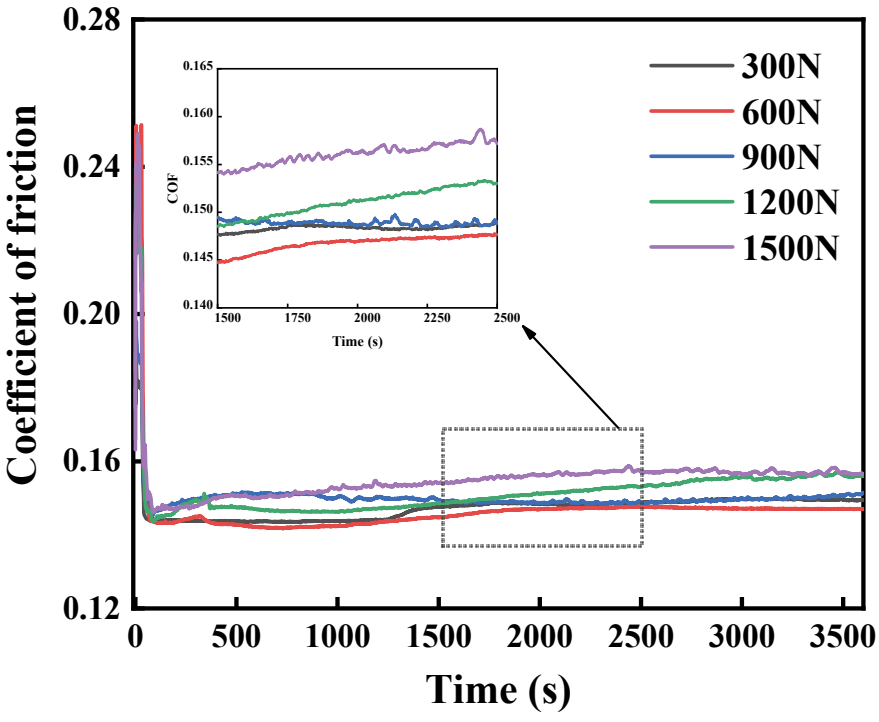


Figure 5. Variation process of friction coefficient under fixed pressure working conditions.

Table 5. The average friction coefficient of corresponding pressure conditions.

Pressure (N)	Minimum COF	Maximum COF	Average COF
300	0.1476	0.1489	0.1484
600	0.1448	0.1478	0.1467
900	0.1484	0.1498	0.1489
1200	0.1485	0.1534	0.1511
1500	0.1540	0.1587	0.1561

As shown in Figure 5 and Table 5, the friction coefficient decreases with the increasing load at lower loads. This phenomenon is mainly related to the following two reasons:

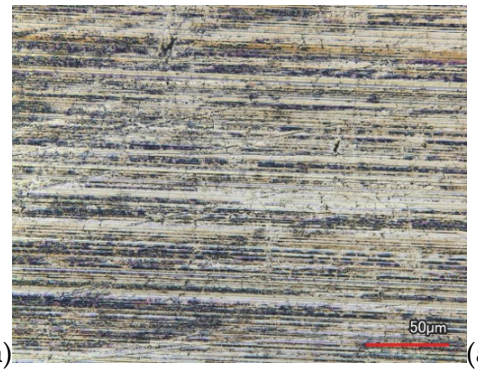
(1) (At 190 °C, the low viscosity of lubricating oil leads to the existence of micro-convex contact in the friction state. However, the number of rough peak contacts is low, and the actual contact area of the friction surface is small at lower loads. According to the mechanism of pressure on friction, the actual frictional contact area S is proportional to the two-thirds power of the pressure between the friction pairs, so the proportion of the increase in contact area is much smaller than the proportion of the increase in load, which means the proportion of the increase in the force of friction is also smaller than the proportion of the increase in pressure;

(2) When the load increases, the contact area of the rough peak increases, and the additives in the lubricating oil contact with the metal surface and form a friction reaction film, thus producing a certain antifriction effect.

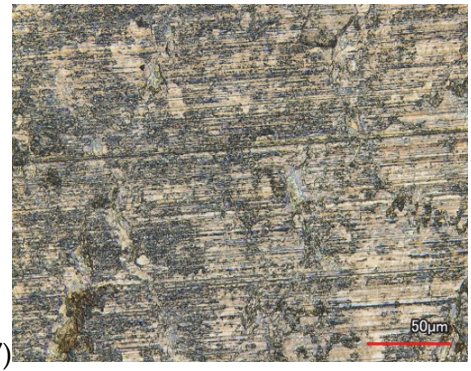
With the further increase in load, when the load reaches 900 N or more, the effect of the friction-reducing substances in the lubricant on the friction coefficient is smaller than the increase in friction force with the increase in load, thus making the trend of friction coefficient change from decreasing to increasing after the friction pair enters the higher load condition.

4.2. Micromorphology Under Different Working Conditions

Figure 6 shows the micromorphology of cylinder liners and piston rings after friction at 80 °C, 110 °C, 140 °C, and 190 °C. From Figure 6, the microscopic morphology of the cylinder liners after friction was dominated by friction marks. In the microstructure of the piston rings, the original microcrack structure was enlarged to form a dotted or reticulated porous structure on the outer surface of the piston rings after the special process of chromium plating technology. The S_a of the microstructure of the cylinder liner and piston ring in the constant temperature tests are shown in Table 6. The surface roughness of the cylinder liner was significantly higher in the high temperature condition than in the low temperature condition, while the surface roughness of the piston ring did not show a clear pattern with the friction temperature.



(**a**)



(**a′**)

Figure 6. *Cont.*

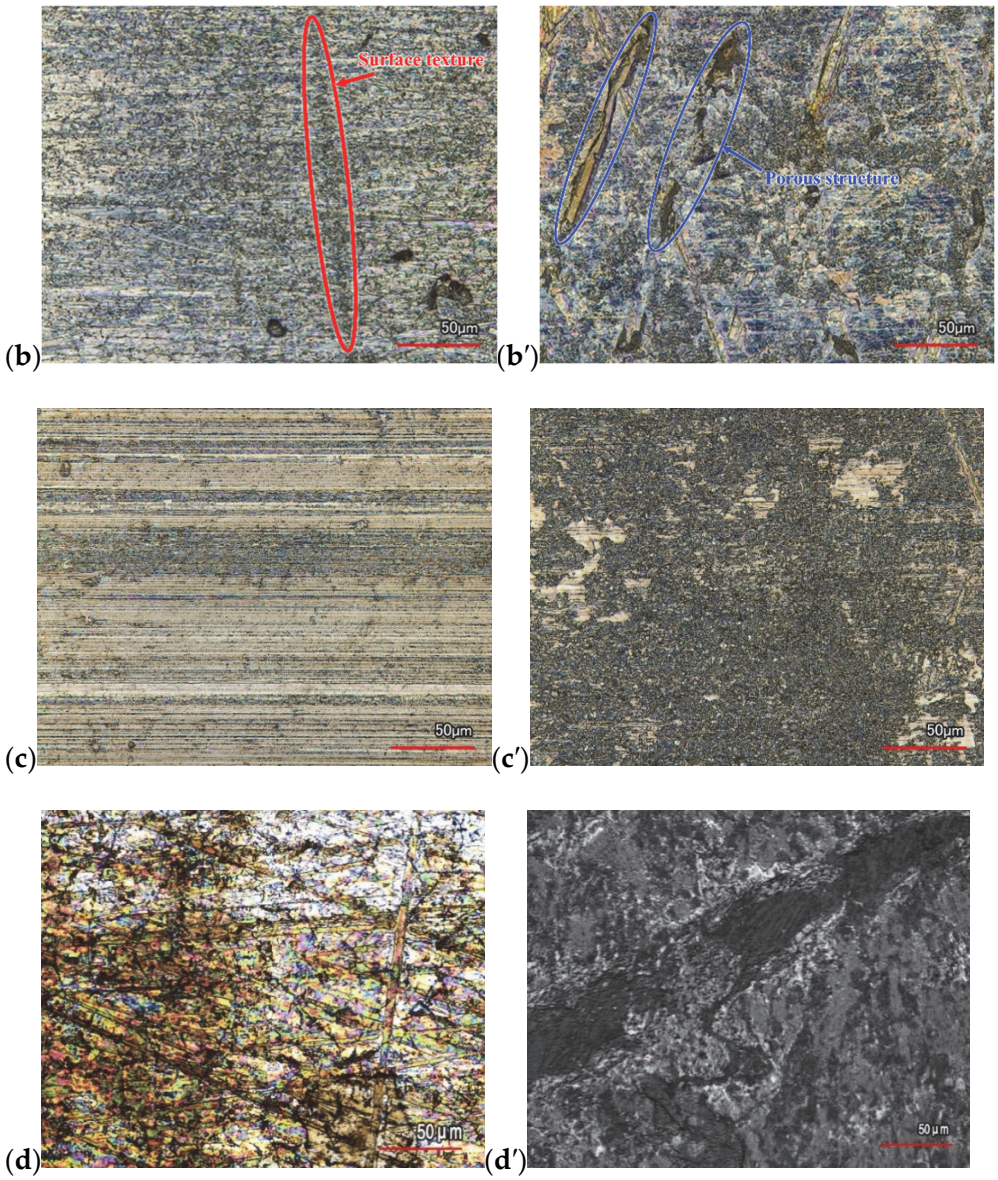


Figure 6. Images acquired with the VK-150K 3D laser microscopic imager, (**a**–**d**) 2D micromorphology images of cylinder liners, and (**a′**–**d′**) micromorphology images of piston rings at different friction temperatures: (**a**) 80 °C, (**b**) 110 °C, (**c**) 140 °C, and (**d**) 190 °C.

Table 6. Surface roughness at different temperature working conditions.

Temperature (°C)	S_a (μm)	
	Cylinder Liner	Piston Ring
80	0.0089	0.1448
110	0.0107	0.2079
140	0.0097	0.1880
190	0.0141	0.2852

Figure 7 shows the micromorphology of cylinder liners and piston rings under different pressure conditions, and the microscopic morphology under 1200 N is shown in Figure 6d,d′ for 190 °C. The S_a of the microstructure of the cylinder liner and piston ring in the constant pressure tests are shown in Table 7.

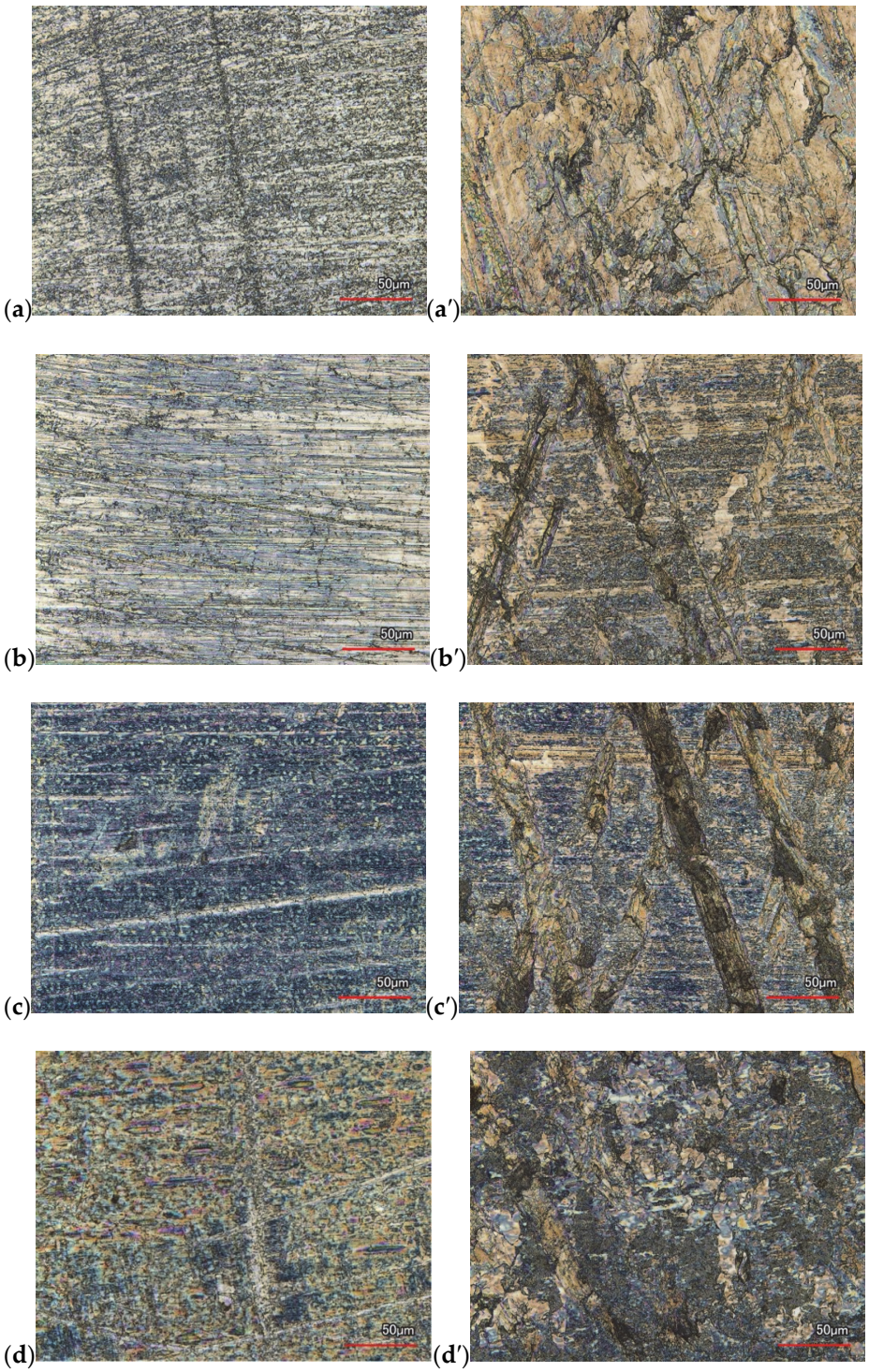


Figure 7. Images acquired with the VK-150K 3D laser microscopic imager, (**a**–**d**) 2D micromorphology images of cylinder liners, and (**a**′–**d**′) micromorphology images of piston rings at different friction pressures: (**a**) 300 N, (**b**) 600 N, (**c**) 900 N, and (**d**) 1500 N.

From Figure 7a–d, there are several obvious parallel distributions of "gully" shape in the micromorphology of the cylinder liner at 300 N. These features are the original surface texture of the cylinder liner surface. Due to less wear at the corresponding pressure of 300 N, the textural features of the surface weave were retained more on the microscopic surface of the friction contact surface. As the load increases, the parallel distribution of the "gully" shape is gradually replaced by dense friction marks.

Table 7. Surface roughness at different pressure working conditions.

Pressure (N)	S_a (μm)	
	Cylinder Liner	Piston Ring
300	0.01371	0.4645
600	0.01142	0.3749
900	0.00989	0.7570
1200	0.01413	0.2852
1500	0.01545	0.2595

The distribution of the overall contour of the piston ring was highly variable in Figure 7a′–d′, primarily due to the prominence of the "reticulate" porous organization of the surface, although there is a clear distribution of friction marks on the low-gradient surface regions. But, the overall wear level is not enough to make the friction marks cover the original microcrack structure.

5. Fractal Characterization of PSD Method

5.1. Variation of Fractal Dimension with Temperature

Figure 8 shows the bilogarithmic plot after processing with the PSD method. The bilogarithmic curves of the power spectral density and spatial frequency of the three-dimensional microform are folded lines, and each linear section in the curve corresponds to a different fractal dimension. A frequency range was selected in the bilogarithmic plot so that the data on the relationship between the variation of power spectral density and frequency was linearly regressed to obtain the slope of the fitted curve.

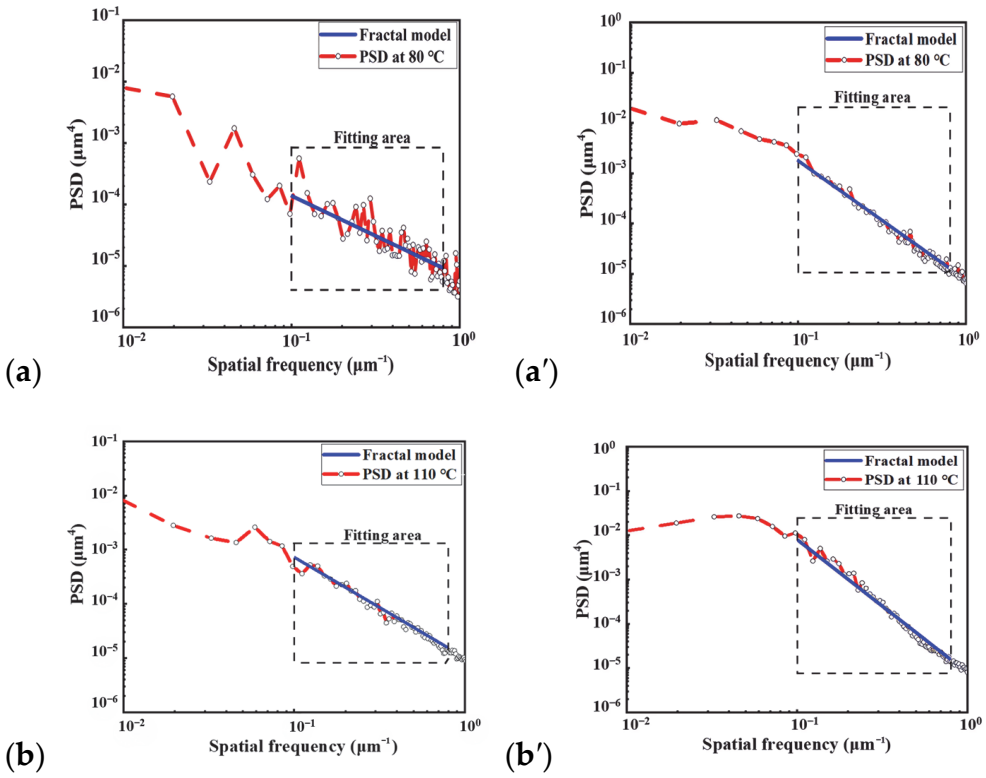


Figure 8. *Cont.*

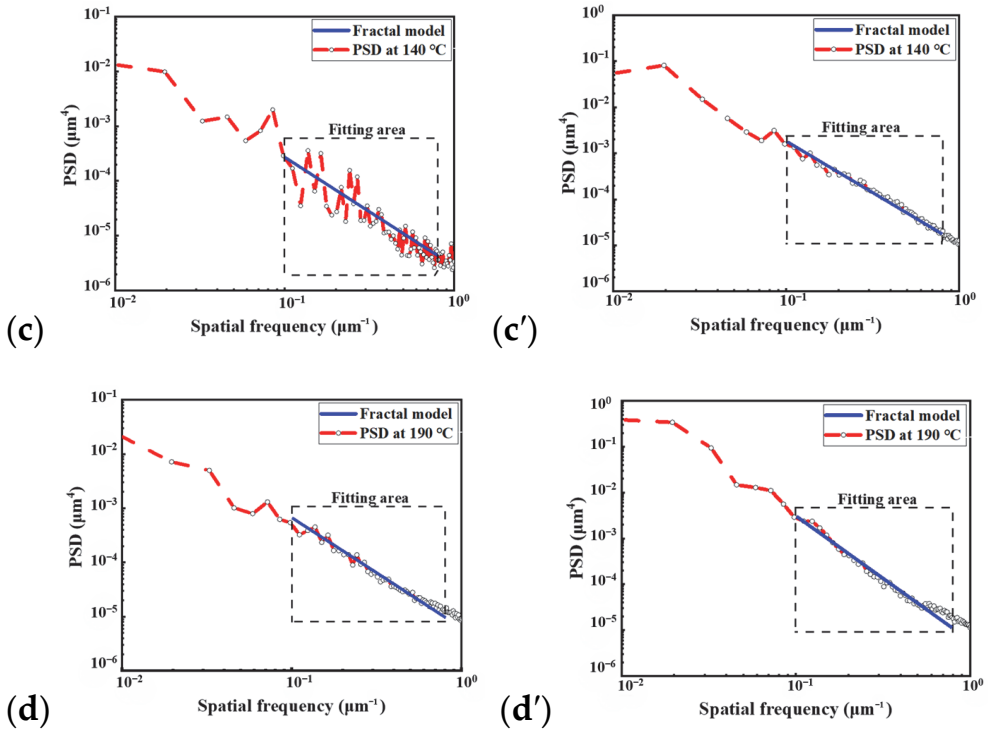


Figure 8. Evolution of spectral power density with the spatial frequency of micromorphology measured at different frictional temperatures. The red line represents the power spectral density at the corresponding temperature. The blue line indicates the fractal fitting, and the dashed area marked in the graph denotes the fitting region. (**a**–**d**) Cylinder liners and (**a′**–**d′**) piston rings.

Table 8 shows the characterization parameters of micromorphology under various temperature conditions. In the constant temperature condition of 110 °C, the initial calculated value of the fractal dimension was 2.857, and the initial calculated value of the Sa was 0.0128 μm, which was higher than the 80 °C and 140 °C conditions. Combined with the three-dimensional microscopic profile of the cylinder liner at 110 °C under constant temperature, there is a distinctly raised profile distribution in the area of the x-range μm and y-range [129.9, 135.2] μm, and its peak height is 0.453 μm. The reason for its high peak is that the profile acquisition equipment uses an optical measurement principle, which is affected by the reflectivity of the detection surface. The peak height is 0.453 μm, and its high peak height is mainly due to the optical measurement principle of the profile acquisition equipment, which is affected by the reflectivity of the detection surface. The reason for the high height of the profile is the systematic error in the measurement, and the existence of this error has a large impact on the roughness calculation. After the correction of the ranks in this area, the calculated roughness *Sa* was 0.0107, while the calculated value of the fractal dimension was 2.868, which was not a significant difference from the uncorrected one.

Table 8. Characterization parameters of micromorphology under various temperature conditions.

Temperature (°C)	Cylinder Liner			Piston Ring		
	β	D_f	S_a (μm)	β	D_f	S_a (μm)
80	−1.172	2.914	0.0089	−2.811	2.0945	0.0145
110	−1.264	2.868	0.0107	−2.726	2.137	0.0208
140	−1.693	2.654	0.0097	−2.202	2.399	0.0198
190	−2.095	2.452	0.0141	−2.596	2.202	0.0285

Figure 9a shows the relationship between the variation of fractal dimension, surface roughness, and friction coefficient of the micromorphology of the cylinder liner at different temperature conditions. In the three temperature conditions between 80 and 140 °C, the fractal dimension value decreased with the increasing temperature, but the decreasing trend was slow. As the fractal dimension decreased, the local peaks and valleys of the morphology were obvious, and this feature was also reflected in the friction morphology at 190 °C. The corresponding calculated value of the fractal dimension was 2.404, which is consistent with the variations in fractal dimension and morphological characteristics.

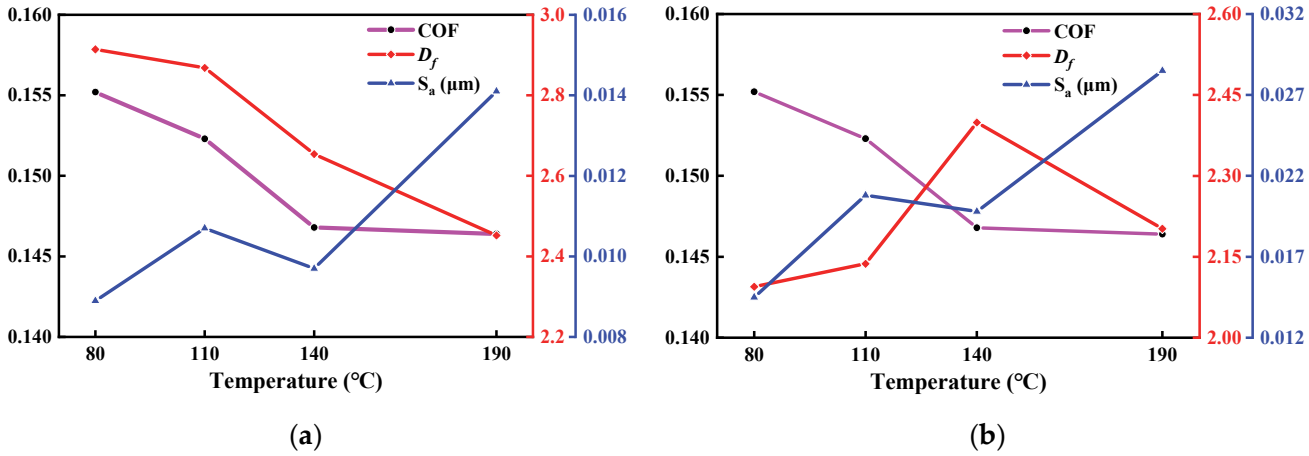


Figure 9. Characterization parameters of the morphology at corresponding temperature conditions; (**a**) cylinder liner and (**b**) piston rings.

In addition, the microscopic morphology of the piston rings exhibited a similar pattern in the relevant parameters at different temperatures. In the microscopic morphology of the piston ring shown in the Figure 9b, the overall characteristics of the surface morphology of the piston ring are all dominated by the obvious porous organization due to the surface treatment process. Therefore, the variation of its surface roughness and fractal dimension depends mainly on the friction marks and the microcrack structure of the chromium-plated crystal layer.

5.2. Variation of Fractal Dimension with Pressure

The logarithmic relationships between the power spectral density and the frequency of the cylinder liners and piston rings after the PSD method are shown in Figure 10. At a pressure of 300 N, the friction contact surface retains more textural features of surface weaving on its microscopic surface due to the small degree of wear, which makes the calculated value of fractal dimension lower. As the pressure increased and the wear level intensified, the generated friction marks gradually covered the original weave features and their self-similarity increases, making the fractal dimension of the morphology at 600 N and 900 N conditions larger than that at 300 N. When the pressure increased further, the surface wear increased and new friction marks and roughness peaks were generated under higher pressure, which made the self-similarity of the morphology decrease and the fractal dimension decrease. As shown in Table 9, the variations in surface roughness and fractal dimension also showed a certain regularity: the Sa value was larger at low load and showed a tendency to decrease and then increase with the increase in pressure.

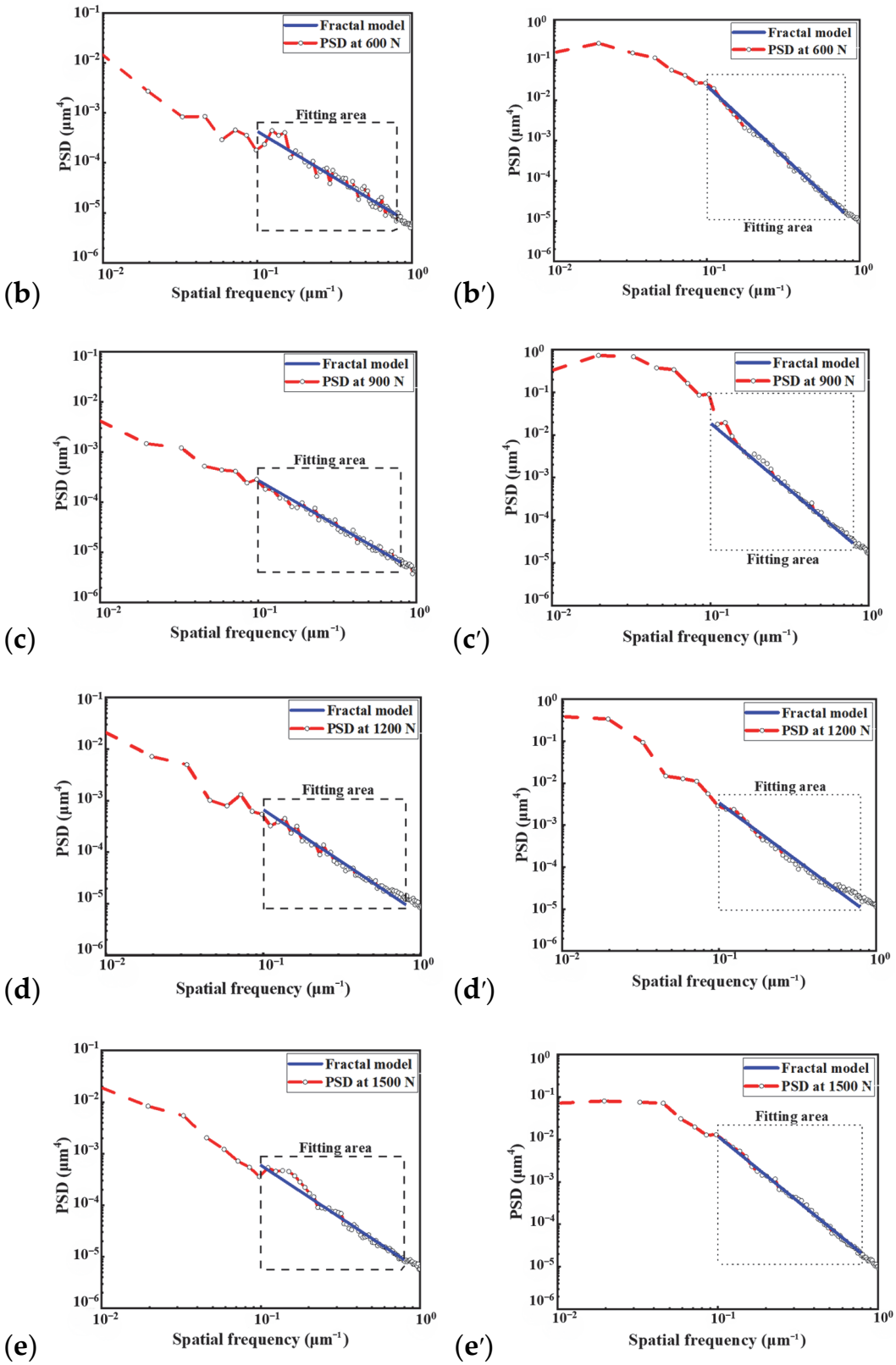


Figure 10. Evolution of spectral power density with the spatial frequency of micromorphology measured at different frictional pressures. The red line represents the power spectral density at the corresponding temperature, the blue line indicates the fractal fitting, and the dashed area marked in the graph denotes the fitting region. (**a**–**e**) Cylinder liners and (**a′**–**e′**) piston rings: (**a**) 300 N, (**b**) 600 N, (**c**) 900 N, (**d**) 1200 N and (**e**) 1500 N.

Table 9. Characterization parameters of micromorphology under various pressure conditions.

Pressure (N)	Cylinder Liner			PISTON Ring		
	β	D_f	S_a (μm)	β	D_f	S_a
300	−1.814	2.593	0.0137	−3.418	2.372	0.0465
600	−1.267	2.867	0.0114	−4.712	2.601	0.0375
900	−1.619	2.691	0.0099	−3.397	2.514	0.0757
1200	−2.095	2.453	0.0141	−2.596	2.000	0.0285
1500	−2.025	2.488	0.0155	−3.108	2.633	0.0259

From Figure 11b, there was no significant correlation change between the fractal dimension, roughness, and friction coefficient of the piston ring morphology. Since the microscopic morphology of the piston ring had obvious local characteristics, the regularity between the surface fractal dimension and roughness was not obvious in the pressure test data set.

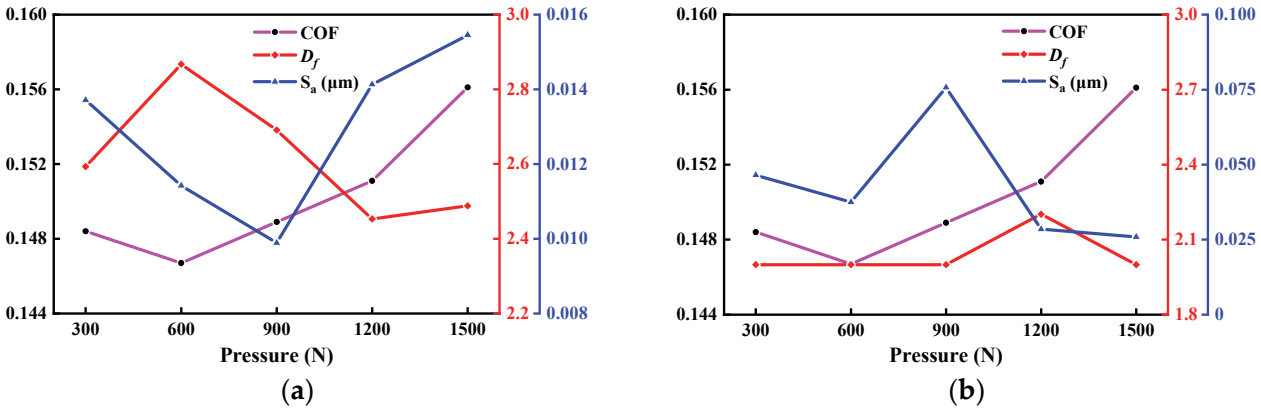


Figure 11. Characterization parameters of the morphology at corresponding pressure conditions. (**a**) Cylinder liner and (**b**) piston rings.

Figures 7 and 9 primarily compare the friction coefficient, fractal dimension, and surface roughness. Among these, the friction coefficient is not only related to the morphological characteristics but is also influenced by the lubricant properties. Thus, it does not exhibit a direct correlation with the other two parameters. In contrast, the fractal dimension and surface roughness, both being morphological characterization parameters, demonstrate a certain degree of correlation. The experimental results reveal an approximately inverse relationship between roughness and fractal dimension. When the roughness is higher, the peaks and valleys of the microscopic surface become more pronounced, indicating distinct local features. The fractal dimension, on the other hand, reflects the self-similarity of the surface—the consistency between local and global characteristics. When the local features are more prominent, the fractal dimension tends to be lower.

6. Conclusions

This study attempts to present the effect of friction temperature and pressure on the microscopic morphology of a cylinder liner and piston ring by fitting a fractal model using the PSD method. The friction coefficients and micromorphology of cylinder liners and piston rings under various conditions were obtained by simulating different temperature and pressure working conditions of internal combustion engines with the SRV friction test machine. The data from the PSD method obtained after processing the micromorphology was fitted into the fractal model to obtain the fractal and roughness parameters. The processing results of the fixed temperature experiment show that, within 80–140 °C, the

increase in temperature and decrease in lubricant viscosity make the rough peak contact increase and the micro-morphology become more complex. When the temperature rises to 190 °C, due to the phenomenon of lubricant degradation and coking of the friction contact surface, the friction conditions are more severe. As the distribution of friction marks on its surface is more complex, the fractal dimension is reduced while its surface roughness also increases. In the lower-pressure conditions, the surface morphology of the cylinder liner is dominated by the original surface weave. Due to the interlaced friction patterns and surface textures, the fractal dimension grew and the roughness reduced as the pressure increased. When the pressure reached 1200 N or more, the surface roughness tended to increase and the fractal dimension decreased. The surface roughness tended to rise and the fractal dimension fell.

The relevant parameters of the piston ring also showed a similar regular variation to the cylinder liner. The calculation of fractal dimension and roughness was also affected when the surface of the microform had a machining structure with a large gap between the scale and friction marks.

In this study, fractal theory is primarily applied to characterize the surface morphology of friction pairs at microscopic scales. Building upon this foundation, we can further integrate fractal theory with the established morphological evolution patterns under varying temperature and pressure distributions to develop a fractal contact model. This model will facilitate friction simulation calculations to investigate the influence of the relevant fractal parameters on contact stiffness and damping characteristics.

Author Contributions: Methodology, X.L. and M.L.; software, validation, data curation, writing original draft preparation, X.L. and X.C.; formal analysis, writing review and editing, X.L., X.C., X.M. and M.L.; funding acquisition, X.L. and M.L. All authors have read and agreed to the published version of the manuscript.

Funding: This work was supported by the Natural Science Foundation of Hebei Province (E2022202026) and the National Science Foundation of China (52005149).

Data Availability Statement: Data are contained within the article.

Acknowledgments: We would like to express our appreciation to the colleagues in our research group.

Conflicts of Interest: Author Xuan Ma was employed by the company Caterpillar (China) Co., Ltd. The remaining authors declare that the research was conducted in the absence of any commercial or financial relationships that could be construed as a potential conflict of interest.

Nomenclature

CL-PR	Cylinder liner–piston ring
COF	Coefficient of friction
PTFE	Polytetrafluoroethylene
ZDDP	Zinc dialkyl dithiophosphate
PSD	Power spectral density
APSD	Area power spectral density
D	Fractal dimension
W-M	Weierstrass–Mandelbrot fractal function
Sa	Surface roughness
$S(r)$	The number of non-empty boxes
Q	Morphological measure
δ	Measurement scale
$P(f)$	Power spectral density
f	Frequency
DFT	Discrete Fourier transform

M	The number of sampling points in the x direction
N	The number of sampling points in the y direction
Tx	Fixed sampling interval in the x-direction
T_y	Fixed sampling interval in the y-direction
α	Fitting parameter
β	Fitting parameter
$z(x, y)$	The height value of the profile at (x, y)
L	Sampling length
G	Scale factor
γ	Characteristic parameter
R	Number of protruding folds on the constructed surface
n	Frequency index
$\phi(m, n)$	Random phase
Ds	Theoretical fractal dimension

References

1. Gussmagg, J.; Maier, M.; Pusterhofer, M.; Grün, F. EHD simulation study on the influence of measured ICE compression piston ring profiles on the lubrication film formation. *Tribol. Int.* **2024**, *199*, 110015. [CrossRef]
2. Atulkar, A.; Pandey, R.K.; Subbarao, P.M.V. Role of textured piston rings/liners in improving the performance behaviours of IC engines: A review with vital findings. *Surf. Topogr. Metrol. Prop.* **2021**, *9*, 023002. [CrossRef]
3. Guo, P.; Yan, Z.; Xu, J.; Shen, Y.; Wang, J. Wear life prediction of piston ring and cylinder liner based on integration of experiment and bench test data. *Eng. Fail. Anal.* **2024**, *161*, 108259. [CrossRef]
4. Zhang, H.; Gong, J.; Liu, X.; Sun, W.; Sun, K.; Bai, S. Influence of Liner Surface with Parameterized Pit Texture on the Friction Characteristics of Piston Rings. *Processes* **2024**, *12*, 572. [CrossRef]
5. Shahmohamadi, H.; Rahmani, R.; Rahnejat, H.; Garner, C.P.; King, P.D. Thermo-mixed hydrodynamics of piston compression ring conjunction. *Tribol. Lett.* **2013**, *51*, 323–340. [CrossRef]
6. Cheng, D.K.; Liu, X.R. Influence of structural temperature on frictional power Loss of piston ring-cylinder liner system. In Proceedings of the SAE 2017 International Powertrains, Fuels & Lubricants Meeting, Beijing, China, 30 October 2017.
7. Rahmani, R.; Rahnejat, H.; Fitzsimons, B.; Dowson, D. The effect of cylinder liner operating temperature on frictional loss and engine emissions in piston ring conjunction. *Appl. Energy* **2017**, *191*, 568–581. [CrossRef]
8. Du, C.; Sheng, C.; Liang, X.; Rao, X.; Guo, Z. Effects of temperature on the tribological properties of cylinder-liner piston ring lubricated with different oils. *Lubricants* **2023**, *11*, 115. [CrossRef]
9. Wolff, A. Influence of sliding surface roughness and oil temperature on piston ring pack operation of an automotive IC engine. In Proceedings of the Scientific Conference on Automotive Vehicles and Combustion Engines, Poland, Cracow, 22–23 September 2016.
10. Zhang, X.; Li, Y.; Li, M.; Zhang, G.; Liu, X. Coupling of heat transfer and lubrication of cylinder liner-piston skirt conjunction and low-friction temperature strategy of cylinder liner. *Ind. Lubr. Tribol.* **2022**, *74*, 645–653. [CrossRef]
11. Valiente-Blanco, I.; Perez-Diaz, J.L.; Perez-del-Alamo, J.L.; Diez-Jimenez, E. Temperature Dependence of the Friction Coefficient of Grease-Lubricated PTFE Linear Bushings Against Titanium Grade 5 Alloy (Ti_6Al_4V) and Life Tests Operating at High-Speed. *J. Tribol.* **2020**, *142*, 091701. [CrossRef]
12. Lyu, X.; Hu, J.; Wang, Y.; Sheng, J.; Ma, X.; Li, T.; Ge, C. Effect of temperature on tribofilm growth and the lubrication of the piston ring-cylinder liner system in two-stroke marine engines. *Friction* **2024**, *12*, 1858–1881. [CrossRef]
13. Kanemoto, K.; Ito, A. A study on the effect of factors of piston motion on the piston ring rotation of an engine. *Tribol. Int.* **2024**, *194*, 109483. [CrossRef]
14. Lyu, B.; Meng, X.; Wang, C.; Cui, Y.; Wang, C. Piston ring and cylinder liner scuffing analysis in dual-fuel low-speed engines considering liner deformation and tribofilm evolution. *Int. J. Engine Res.* **2024**, *25*, 1776–1798. [CrossRef]
15. Shen, Y.; Li, Q.; Liu, Z.; Ye, B.; Fan, J.; Xu, J. Influence of different loads and temperatures on solid lubricant-filled micro-dimples existing on both cylinder liner and piston ring. *Wear* **2023**, *526*, 204926. [CrossRef]
16. Bewsher, S.; Leighton, M.; Mohammadpour, M.; Rahnejat, H.; Offner, G.; Knaus, O. Boundary friction characterisation of a used cylinder liner subject to fired engine conditions and surface deposition. *Tribol. Int.* **2018**, *131*, 424–437. [CrossRef]
17. Zhang, B.; Ma, X.; Liu, L.; Morina, A.; Lu, X. Sliding wear mechanisms and speed-load wear map of cylinder liner and piston ring under lubricated conditions. *Wear* **2025**, *564–565*, 205701. [CrossRef]
18. Li, T.; Wu, J.; Ge, C.; Wang, L.; Yu, Y.; Ma, X.; Qiao, Z.; Tang, H. Molecular dynamics investigation on micro-friction behavior of cylinder liner-piston ring assembly. *Tribol. Lett.* **2023**, *71*, 78. [CrossRef]

19. Baby, A.K.; Rajendrakumar, P.K. Comparative Study on the tribological performance and wear behaviour of hypereutectic Al–Si cylinder liner surfaces textured using micro-drilling and mechanical indentation-based approaches. *Wear* **2024**, *540*, 205240. [CrossRef]
20. Esen, M.; Yilmaz, A.C. Crystalline Carbon Deposition on Piston Ring Substrates and Its Effects on Tribological Characteristics, Engine Performance, and Emissions. *Adv. Eng. Mater.* **2024**, *26*, 2401754. [CrossRef]
21. Zhang, B.; Ma, X.; Liu, L.; Yu, H.; Morina, A.; Lu, X. Study on the sliding wear map of cylinder liner−piston ring based on various operating parameters. *Tribol. Int.* **2023**, *186*, 108632. [CrossRef]
22. Liu, Z.; Shen, Y.; Liu, J.; Qu, J.; Xu, J.; Li, C. Effects of double-sided textures matching on friction and wear performance in reciprocating contact interface. *Wear* **2024**, *556*, 205522. [CrossRef]
23. Lang, S.; Zhu, H.; Wang, Y. Design of parameters for running-in cylinder liner piston rings based on running-in attractor. *Ind. Lubr. Tribol.* **2024**, *77*, 192–201. [CrossRef]
24. Yu, X.; Sun, Y.; Liu, M.; Wu, S. Analytical description of the wear process using a multi-stage contact fractal approach. *Wear* **2024**, *548–549*, 205364. [CrossRef]
25. Cheng, Y.; Wan, Z.; Bu, Y.; Xiong, W.; Long, Y. Normal Contact Model of Fractal Surfaces Considering Friction and Asperity Interactions. *Int. J. Appl. Mech.* **2024**, *16*, 2450057. [CrossRef]
26. Zhang, S.; Li, Y.; Wang, G.; Qi, Z.; Zhou, Y. A novel method for calculating the fractal dimension of three-dimensional surface topography on machined surfaces. *Chaos Solitons Fractals* **2024**, *180*, 114573. [CrossRef]
27. Jain, R.; Pitchumani, R. Fractal Model for Wettability of Rough Surfaces. *Langmuir* **2017**, *33*, 7181–7190. [CrossRef] [PubMed]
28. Feng, W.; Chu, X.; Hong, Y.; Deng, D. Surface Morphology Analysis Using Fractal Theory in Micro Electrical Discharge Machining. *Mater. Trans.* **2017**, *58*, 433–441. [CrossRef]
29. Mahmood, M.A.; Tsai, T.Y.; Hwu, Y.J.; Lin, W.-J.; Liu, L.-C.; Lai, J.-Y.; Pan, J.-W.; Li, W.-L.; Lin, J.-F. Effect of fractal parameters on optical properties of cold rolled aluminum alloy strips with induced surface deflection: Simulations and experimental correlations. *J. Mater. Process. Technol.* **2019**, *279*, 116554. [CrossRef]
30. Zhao, Y.; Luo, Y.; Zhang, Z.; Zhang, H.; Guo, X.; Wang, S.; Cui, H.; Zhang, Y. Fractal Dimension Characterization of Joint Surface Morphology on Dissimilar Friction Stir Lap Welding of Al/Mg. *Materials* **2019**, *12*, 3941. [CrossRef]
31. Wang, Y.; Gang, L.; Liu, S.; Cui, Y. Coupling Fractal Model for Fretting Wear on Rough Contact Surfaces. *J. Tribol.* **2021**, *143*, 091701. [CrossRef]
32. Eftekhari, L.; Raoufi, D.; Eshraghi, M.J.; Ghasemi, M. Power spectral density-based fractal analyses of sputtered yttria-stabilized zirconia thin films. *Semicond. Sci. Technol.* **2022**, *37*, 105011. [CrossRef]
33. Niu, C. Characterization on Wear Surface Topography of Cylinder Liner Based on Fractal Theory. Master's Thesis, Xi'an University of Technology, Xi'an, China, 2021.
34. Liu, H.; Xie, H.; Wu, F.; Li, C.; Gao, R. A novel box-counting method for quantitative fractal analysis of three-dimensional pore characteristics in sandstone. *Int. J. Min. Sci. Technol.* **2024**, *34*, 479–489. [CrossRef]
35. Yan, W.; Komvopoulos, K. Contact analysis of elastic-plastic fractal surfaces. *J. Appl. Phys.* **1998**, *8*, 3617–3624. [CrossRef]
36. Mandelbrot, B.B.; Wheeler, J.A. The Fractal Geometry of Nature. *Am. J. Phys.* **1983**, *51*, 286–287. [CrossRef]

Disclaimer/Publisher's Note: The statements, opinions and data contained in all publications are solely those of the individual author(s) and contributor(s) and not of MDPI and/or the editor(s). MDPI and/or the editor(s) disclaim responsibility for any injury to people or property resulting from any ideas, methods, instructions or products referred to in the content.